Journal of Materials Processing Tech. 328 (2024) 118405

Contents lists available at ScienceDirect

Journal of Materials Processing Tech.

journal homepage: www.elsevier.com/locate/jmatprotec

Unravelling the intricacies of micro-nonuniform heating in field-assisted sintering of multiphase metallic microstructures

Tomaž Tomše [a,*], Benjamin Podmiljšak [a], Lavinia Scherf [b], Reto Kessler [b], Spomenka Kobe [a,c], Andraž Kocjan [a], Sašo Šturm [a,c], Kristina Žužek [a,c]

[a] Jožef Stefan Institute, Department for Nanostructured Materials, Jamova cesta 39, Ljubljana SI-1000, Slovenia
[b] ABB Corporate Research Center, Segelhofstrasse 1K, Baden-Daettwil, CH-5405, Switzerland
[c] Jožef Stefan International Postgraduate School, Jamova cesta 39, Ljubljana SI-1000, Slovenia

ARTICLE INFO

Keywords:
FAST/SPS
Micro-nonuniform heating
Hot spots
Metallic powders
Field-assisted sintering

ABSTRACT

Micro-nonuniform heating in the field-assisted sintering (FAST) of electrically conductive powders has been a topic of discussion in the materials science community. Microstructural specifics, such as neck formation at low consolidation temperatures and density variations, have previously been ascribed to local overheating at the particle-particle contacts due to the Joule effect. However, recent theoretical modelling studies suggest that the very fast diffusion of heat within the micron-sized particles prevents the overheating, thereby challenging the conventional understanding of FAST-related heating effects. To provide a new experimental perspective on the local overheating and underscore its pivotal role in controlling the microstructure formation, we have studied the phase transformations in a Nd-Fe-B-type multiphase metallic powder during FAST. The formation of the α-Fe phase, following the peritectic decomposition of the $Nd_2Fe_{14}B$ matrix phase expected at ≈1180 °C (T_{PER}), was observed for FAST temperatures (T_{FAST}) below T_{PER}. A correlation between the electric current and the final phase composition, which can only be explained by considering the local overheating effect, was established. We showed that the formation of the α-Fe phase at $T_{FAST} < T_{PER}$ can be mitigated by (i) decreasing the electric current through the sample, which is achieved by lowering the heating rate from 100 to 10 °C/min or by using electrically highly conductive pressing tools (WC) and a non-conductive coating (BN), or by (ii) interparticle necking achieved through a thermal pre-treatment of the powder compact that decreases the overall resistance. Our findings emphasize the criticality of the electric current modulation to minimize any undesired phase transformation, paving the way for future developments in rapid, FAST-based strategies aimed at refining the microstructures and tailoring the properties of multiphase metallic materials.

1. Introduction

In the drive to develop new materials or to improve the properties of existing ones, rapid sintering can consolidate powders into fully dense bodies. Field-assisted sintering technology (FAST), also known as spark-plasma sintering (SPS) or pulsed-electric-current sintering (PECS), is an electrical current-activated, pressure-assisted technique that offers faster heating rates (several hundred K/min), lower processing temperatures, and shorter heating cycles than conventional approaches. Such conditions are advantageous for ensuring a high density, a finer and more homogeneous microstructure, improved mechanical properties, and for tailoring the functional properties like the electrical conductivity, ferroelectric, optical, and magnetic characteristics of the final products (Orru et al., 2009). FAST-based techniques have been used for the synthesis of a wide range of ''hard-to-sinter'' materials and materials that exhibit a strong structure-properties dependence, for example, ultra-high-temperature ceramics, refractory metals, alloys, composites, polymers, and nanostructured materials (Guillon et al., 2014). Furthermore, the final geometry of the products prepared by FAST is defined by the design and dimensions of the pressing tools, which makes FAST a near-net-shape technique with the potential for the manufacture of complex shape products, e.g., spheres and turbine blades, as demonstrated by Maniere et al. (2017).

In FAST the principal mechanisms governing densification, such as grain-boundary and lattice diffusion, and plastic deformation, can be ascribed to the mechanical (compressive stress and creep) and thermal

* Corresponding author.
E-mail address: tomaz.tomse@ijs.si (T. Tomše).

https://doi.org/10.1016/j.jmatprotec.2024.118405
Received 16 January 2024; Received in revised form 10 March 2024; Accepted 7 April 2024
Available online 9 April 2024

(high heating rates, temperature distribution, and temperature gradients) effects (Guillon et al., 2014). Concerning the distribution of the electric currents in the setup, the majority of the current flows through the sample if the latter is electrically more conductive than the die (Vanmeensel et al., 2005). As proposed by several authors, the Joule heating effect, which occurs at the particle-particle contacts, leads to local overheating before the necks are formed, i.e., when the current density at the contacts is high. The term ''hot spots'' often appears in the literature. The first notable example is the work of Nowak et al. (Nowak et al., 2011) who observed nanoprecipitates (<50 nm in diameter) in bulk $Zr_{57}Cu_{20}Al_{10}Ni_8Ti_5$ metallic glass samples, which the authors attributed to the partial devitrification in the neck regions due to local overheating. The second example is the paper of Schwesig et al. (Schwesig et al., 2011) who observed density fluctuations on the micrometre scale with a network-like pattern in FAST samples prepared from silicon nanoparticles. The authors correlated these fluctuations with the percolation current paths through the sample using theoretical modelling. Neither of the two papers offers solutions to prevent or minimize the overheating effect. Song et al. (2006) reported on the formation of necks between spherical 15–40 μm Cu particles sintered at low FAST temperatures, which they attributed to overheating and melting of particle-particle contacts, followed by rapid solidification. However, this explanation was later challenged by Tržaška et al. (2019) who proposed that the intense plastic deformation due to large contact stress promotes recrystallization and neck growth.

The hypothesis of micro-nonuniform heating due to the Joule effect was tested by considering the thermal conductivity of the sintered material. Holland et al. (2012) studied the role of thermal conductivity in dissipating temperature differences between the grain boundaries and grain cores for ionic ceramics with large grain boundary resistivity. Using numerical modelling, they showed that the heat dissipation is so fast that any temperature difference becomes insignificant for particles of tens of microns or smaller in size. Collard et al. (2017) performed experimental and theoretical analysis of local heating effects for $Ti_{48}Al_{48}Cr_2Nb_2$ particles of ≈100 μm in size. Any local overheating during FAST would trigger equiaxed to lamellar phase transformation ($\gamma + \alpha 2 \rightarrow \alpha$), which was not observed. Supported by FEM calculations, the authors concluded that significant overheating is improbable. Similar conclusions disproving the overheating in Ti-Al and Ag-Zn systems can be found in (Trzaska et al., 2019). In summary, the phenomenon of micrononuniform heating during FAST remains controversial.

An electrically conductive Nd-Fe-B-type powder is used here as a case study to provide a new experimental perspective on the existence of local overheating caused by the Joule effect. The Nd-Fe-B ternary alloy is the basis for permanent magnets used in numerous high-end applications, e.g., computers and smartphones, magnetic resonance imaging, sensors, and energy-conversion devices such as electric motors and generators (Lewis and Jiménez-Villacorta, 2013). The phase diagram of the Nd-Fe-B ternary system is relatively complex (Matsuura et al., 1985) and two specific phase transformations were considered here. The first is the peritectic reaction at ≈1180 °C (T_{PER}):

$$L(l) + \gamma\text{-Fe(s)} \rightarrow Nd_2Fe_{14}B(s) \quad (1)$$

where $Nd_2Fe_{14}B$ is the hard-magnetic matrix phase. The properitectic soft-magnetic α-Fe phase, a low-temperature allotropic form of iron, is found in the microstructure of Nd-Fe-B alloys unless the material is sufficiently undercooled before the solidification or isothermally annealed to dissolve the precipitated α-Fe (Burzo, 1998). α-Fe is a soft-magnetic phase with a detrimental effect on the magnetic properties (Herbst, 1991). The second reaction is eutectic at ≈665 °C (T_{EUT}):

$$L(l) \rightarrow Nd_2Fe_{14}B(s) + Nd(s) \quad (2)$$

where Nd is the secondary phase found in materials with a Nd content exceeding the stoichiometric $Nd_2Fe_{14}B$ composition. The melting eutectic enables liquid-phase sintering, vital for the manufacture of Nd-Fe-B-type magnets via powder metallurgy (Sagawa et al., 1984).

Considering that a fine-grained microstructure improves the Nd-Fe-B magnets' high-temperature performance (Uestuener et al., 2006), rapid FAST represents an attractive alternative to conventional sintering. However, in our preliminary study, the α-Fe phase was unexpectedly found in bulk Nd-Fe-B samples prepared via FAST at sintering temperatures below T_{PER}, and Joule overheating was suggested as the mechanism behind the decomposition of the matrix phase (Tomše et al., 2020).

In this paper, we report on the relationship between electric current and microstructure formation in the Nd-Fe-B system. Various FAST conditions were employed to prepare fully dense samples without reducing the sintering temperature. The heating power (P) is proportional to the square of the current (I) and the sample's resistance (R):

$$P \alpha I^2 \times R \quad (3)$$

A high current density and a greatly increased resistance at the particle-particle contacts imply an enhancement of the local Joule heating. Considering Eq. (3), two strategies were employed to reduce the overheating effect. The first strategy focuses on reducing electric currents in the sample by decreasing the heating rate or utilizing pressing tools with higher electrical conductivity. The second strategy involves thermal pre-treatment of the powder compact to achieve interparticle necking, thereby reducing particle-particle contact resistance. Both strategies were successfully implemented to prevent the decomposition of the matrix phase, as confirmed through microstructural observation and XRD analysis of FAST samples. This study provides conclusive experimental verification of micro-nonuniform heating based on FAST-induced phase transformations in a complex metallic system and offers practical solutions to mitigate the negative impact of overheating on the microstructure.

2. Experimental procedure

2.1. Nd-Fe-B alloy

The Nd-Fe-B-type powder with composition $Nd_{30.0}Pr_{0.6}Dy_{1.0}Fe_{63.8}Co_{3.0}Ga_{0.2}Cu_{0.1}Al_{0.1}B_{0.9}O_{0.3}$ (wt%) was provided by the company Magneti Ljubljana d.d. The powder was prepared using a standard powder-metallurgy approach: the alloy was strip cast and the flakes were subsequently decrepitated with hydrogen to obtain a coarse and friable powder, which was then jet-milled to a finer, near-monocrystalline, powder with an average particle size of 6.5 μm. Cylindrical powder compacts were prepared by uniaxially pressing the powder in a mould at 100 MPa. The pressure was optimized to achieve a relative density of ≈57 % and sufficient mechanical stability of the compacts. A pulsed magnetic field of 2 T was applied before and during the pressing parallel to the pressing direction to crystallographically align the particles along the tetragonal *c*-axis of the matrix phase, i.e., the easy axis of magnetization. The dimensions of the compacts were 10 mm (diameter) × 10 mm (height).

2.2. Field-assisted sintering (FAST)

The FAST experiments were performed in a Dr. Sinter, Fuji Electronic Industrial Co. Ltd furnace in vacuum (≈5×10^{-2} mbar). A DC current with a 12:2 on-off pulse sequence (12 × 3.3 ms ≈0.04 s of current, followed by 2 × 3.3 ms ≈0.007 s of pause) was applied to heat the Nd-Fe-B powder compact that was placed into a cylindrical die for pressing. 50 MPa of pressure was applied uniaxially on the punches. The dimensions of the die were 40 mm (outer diameter) × 60 mm (height). The outer surface of the die was covered with a thermally insulating graphite felt to minimize the heat loss due to thermal radiation. A K-type thermocouple was inserted into the die at the level of the sample, i.e., in the centre of the die, and the FAST process was temperature controlled. Two types of pressing tools were used: the typical high-strength graphite die

and the custom-made binder-less WC die (NJS Co., Ltd., Japan). Precautions were taken to prevent the Nd-Fe-B from reacting with the die for easier removal of the sintered samples: for the graphite die, a thin graphite foil (≈0.2 mm) was placed between the powder compact and the die/punches; for the WC die, the punches and the inner surface of the die were coated with a BN spray.

Six samples were prepared under different FAST conditions to investigate in detail the micro-nonuniform heating phenomena and its effect on the densification behaviour and the formation of the microstructure. The corresponding process parameters and absolute densities of the as-prepared samples are listed in Table 1. For samples G, G-TP, G-slow, and W, the thermal cycle involved three steps: heating from room temperature to T_{FAST} (step 1 - heating), soaking at T_{FAST} for 10 min, i.e., dwell time (step 2 - isothermal) to ensure full density, and cooling after the power was turned off (step 3 - cooling). All the samples, except for sample G-TP, were prepared from pristine powder compacts. To study the relationship between the interparticle contact resistance and the Joule overheating, sample G-TP was prepared from a powder compact that was thermally pre-treated (partially sintered) before the FAST. The pre-treatment was performed in a tube furnace (Carbolite) in a $\approx 5 \times 10^{-5}$ mbar vacuum at 800 °C for 10 min. This increased the compact's relative density from ≈57–63 %, i.e., to approx. 4.8 g/cm^3. Samples G, G-TP, and W were prepared with a heating rate of 100 °C/min from room temperature to 900 °C, followed by 50 °C/min to the final sintering temperature T_{FAST} to minimize the temperature overshoot. In contrast, sample G-slow was prepared with a heating rate of 10 °C/min to reduce the contribution of the local overheating to the formation of the microstructure by reducing the electric current in the sample. T_{FAST} was set to 950 °C for the graphite die, based on a preliminary investigation (Tomše et al., 2020), and at 1000 °C for the WC die, as further elaborated in Section 4.4. The WC die (sample W) in combination with the BN protective coating was used to reduce the current in the sample without decreasing the heating rate. BN is an electrical insulator and the room-temperature electrical conductivity of WC is roughly two orders of magnitude higher than that of the graphite ($\approx 4.5 \times 10^6$ and 7.6×10^4 S/m, respectively) (Mazo et al., 2022). For comparison, the electrical conductivity of fully dense, metallic, sintered Nd-Fe-B-type material lies in the range 6–9 $\times 10^5$ S/m (Ruoho et al., 2010), between that of graphite and WC. Two additional samples were prepared to study the microstructure formation during FAST at 100 °C/min of heating rate by heating the pristine powder compacts in the graphite die to either 500 or 800 °C (samples G500 and G800, respectively), without a dwell time at T_{FAST}.

2.3. Ram displacement data

For each FAST run, the important process parameters were recorded, i.e., the temperature of the die, the electric current (A), the voltage (V), and the vertical ram displacement (mm) due to shrinkage of the compact and thermal expansion of the setup, i.e., the die, the spacers, and the powder compact. A negative ram displacement corresponds to a thermal expansion and a positive, to a shrinkage. To construct the *displacement curves* (Fig. 8a, Section 3.2.), the ram's displacement was normalized to the maximum value reached at the end of the densification. The first derivatives of the displacement curves, with respect to the temperature, were calculated.

The densification rates for samples G (pristine powder compact) and G-TP (thermally pre-treated compact) were compared to study the contribution of the Joule overheating due to the contact resistance to the densification kinetics. For this purpose, a blank FAST run was performed using the graphite die without a powder compact and the same heating rate (100 °C/min). The ram displacement recorded for the blank run (black curve in Fig. 1) is negative due to the thermal expansion of the graphite and was subtracted from the ram displacement recorded for samples G and G-TP (dashed blue and red curves, respectively), to construct the *shrinkage curves* (Fig. 6b, Section 3.2.), which reflect the true shrinkage and thermal expansion of the powder compact during the FAST. The first derivatives with respect to the temperature were then calculated for the shrinkage curves.

Table 1
FAST conditions and sample densities.

Sample	Powder compact	Pressing tools	Heating rate (°C/min)	T_{FAST} (°C)	Dwell time (min)	Density (g/cm^3)
G	Pristine	Graphite	100 (fast)	950	10	7.65
G-TP	Thermally pre-treated	Graphite	100 (fast)	950	10	7.63
G-slow	Pristine	Graphite	10 (slow)	950	10	7.66
W	Pristine	WC	100 (fast)	1000	10	7.66
G500	Pristine	Graphite	100 (fast)	500	0	/
G800	Pristine	Graphite	100 (fast)	800	0	/

2.4. Characterization

The bulk samples' densities were determined based on the Archimedes' principle. A field-emission-gun scanning electron microscope (FEG-SEM) JEOL JSM-7600 F was used for the microstructural investigation of the Nd-Fe-B powder, of a thermally pre-treated powder compact, and of the bulk FAST samples' cross-sections. For the investigation, the samples were embedded in a resin (EpoFix Kit Resin and hardener from Struers) and metallographically polished with isopropanol-based suspensions of 3-μm and 0.25-μm diamond paste. To observe the major phases, present in the Nd-Fe-B samples, backscattered-electron (BSE) imaging in compositional contrast mode was used. The local chemical composition was determined by energy-dispersive X-ray spectroscopy – EDS (INCA system, Oxford Instruments, UK) point analysis. The XRD analyses of the powder and bulk samples were performed with an X-ray diffractometer (XRD, PANalytical, Netherlands) using Cu–$K_{\alpha 1}$ radiation ($\lambda = 1.5406$ Å). Analyses of the FAST samples were performed on their polished surfaces parallel to the pressing direction.

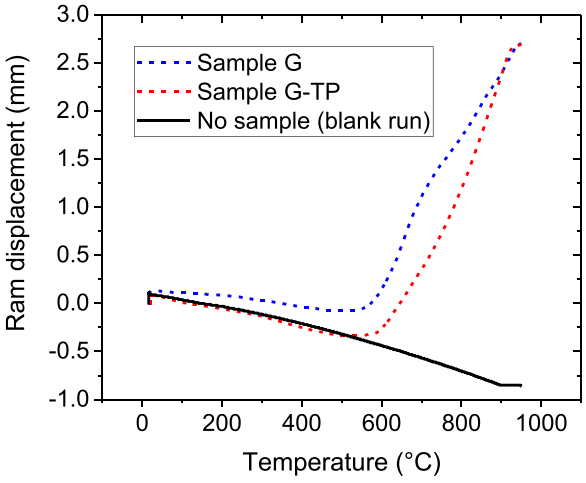

Fig. 1. Ram-displacement data for samples G and G-TP, and a blank run. For FAST runs corresponding to samples G and G-TP, the ram displacement is negative at the beginning of heating, indicating thermal expansion, and becomes positive at higher temperatures due to sample shrinkage. For the FAST run without a sample, i.e., a blank run, the ram displacement is negative throughout heating due to the thermal expansion of the graphite die and spacers.

3. Results

3.1. Microstructural specifics of the Nd-Fe-B material and FAST samples

Backscattered-electron (BSE) mode SEM images of the initial Nd-Fe-B powder are shown in Fig. 2a,b. The dark contrast corresponds to the resin used to embed the powder particles for the microstructural investigation. Most of the powder is near-monocrystalline and composed of irregularly shaped particles up to 10 μm in size. A very small fraction of the powder (estimated at < 1 vol%) contains larger, polycrystalline particles, several tens of microns in size, an example of which is shown in Fig. 2b. The large powder particle has a lamellar structure, typical for a precursor strip-cast Nd-Fe-B-type alloy (Bernardi et al., 1998). This shows that the milling of the hydrogen-decrepitated coarse powder (Section 2.1.) was performed sub-optimally. The microstructure of the thermally pre-treated, i.e., partially sintered compact, used to prepare sample G-TP (Section 2.2.), is shown in Fig. 2c. As seen in the BSE-SEM image, the necks between the powder particles are formed and the pores are mostly interconnected, which is typical for the initial sintering stage (Kang, 2004).

The BSE-SEM images of the bulk FAST samples are shown in Fig. 3a-c (sample G), 3d (sample G-TP), 3e (sample G-slow), and 3 f (sample W). All the samples exhibit a multiphase microstructure, as observed from the compositional contrast, and they are fully dense without any signs of porosity. For sample G, distinguished from the other samples by a phase with dark contrast, the EDS microanalysis was performed at individual locations to probe the chemical compositions of the respective phases (sites 1–4 in Fig. 3b). The grey matrix phase (site 1) is composed of Fe (87.6 at%) and the rare-earth (RE) elements Nd and Dy (11.2 and 1.2 at %, respectively). The Fe to RE atomic ratio is ≈7, corresponding to the stoichiometric $RE_2Fe_{14}B$ hard-magnetic phase where Nd atoms are partially substituted by Dy in the crystal structure (Sagawa et al., 1987). Boron was not quantified with this analysis. The dark phase (site 2) is composed of Fe (98.8 at%), which agrees with the dark contrast in the BSE-SEM image. As reported in an earlier paper, the XRD and EBSD analyses of the FAST samples prepared similarly identified it as the α-Fe phase (Tomše et al., 2020). A small amount of neodymium that was detected and quantified for site 2 (1.2 at%) is likely to be from the surrounding phases, considering the analytical limitation of the EDS technique. Compared with the grey matrix (site 1), grains with brighter contrast (sites 3 and 4) are enriched with neodymium (11.2, 29.9, and 50.8 at% for sites 1, 3, and 4, respectively). Other contributions quantified for sites 3 and 4 include Dy (2.3 and 1.9 at%, respectively), Fe (33.8 and 40.6 at%, respectively), and O (34.0 and 6.7 at%, respectively) elements. Oxygen is an impurity that accumulates in an Nd-Fe-B-type alloy during the production process due to the highly negative reduction potential of the neodymium (-2.32 V) (Schultz et al., 1999). However, the exact chemical compositions of the phases with bright contrast are not easily assessed due to the aforementioned analytical limitation. The phases with compositions rich in neodymium are denoted here as Nd-rich phases.

A detailed SEM analysis of sample G confirmed that its microstructure was largely homogeneous throughout the cross-section. However, the investigation also revealed distinct areas displaying larger elongated grains of the matrix phase and strip-like regions of a bright Nd-rich phase. An example of such a microstructural inhomogeneity is shown in Fig. 3c. The microstructure is comparable to the lamellar structure of a larger powder particle shown in Fig. 2b. Apparently, the characteristic microstructural specifics, i.e., grain shape and phase distribution, of an individual polycrystalline particle, were preserved in sintered sample G. This is attributed to rapid heating, i.e., 100 °C/min, and short dwell time at T_{FAST} (10 minutes). Furthermore, it was observed that the dark α-Fe phase is largely absent in the area corresponding to a large powder particle.

Stereological image analyses were performed to compare the phase fractions between the samples. For sample G, the analysis revealed that it contains approx. 85 % of the matrix phase, 8 % of the Nd-rich phases (including metallic and oxides), and 7 % of the α-Fe phase. In comparison, for samples G-TP, G-slow, and W, the area fraction of the matrix phase is approx. 95 %, the rest being the Nd-rich phases (5 %), while the α-Fe is absent.

The phase composition of the powder and FAST samples was further analysed with X-ray diffraction. X-ray diffraction patterns are shown in Fig. 4. The stick patterns corresponding to the tetragonal $Nd_2Fe_{14}B$ matrix phase (reference code 01–079–1994) and the body-centred cubic (bcc) alpha iron (reference code 00–006–0696) are added for comparison. The $Nd_2Fe_{14}B$ pattern consists of 160 peaks and the peak intensities well match the diffraction pattern recorded for the powder. The FAST samples were prepared from magnetically aligned powder compacts and are crystallographically textured. To avoid reflection from the (006) plane of the matrix phase ($2\Theta \approx 44.6°$), dominant in diffraction patterns taken on surfaces perpendicular to the tetragonal c-axis direction (Liu et al., 2010), XRD analyses were performed on the surfaces parallel to the c-axis alignment. In this way, the peak overlapping with the (110) peak with the highest intensity in the bcc iron pattern ($2\Theta \approx 44.7°$) was prevented.

As further shown in Fig. 5a,b, the majority of reflections correspond to the $Nd_2Fe_{14}B$ phase. Nevertheless, several minor phases were identified in the samples, as indicated in Fig. 5a ($2\Theta = 24–37°$ range): cubic Nd_2O_3 - reference code 03–065–3184, cubic $NdPrO_3$ - reference code PDF 00–052–1438, and cubic $DyC_{0.4}$ - reference code 01–073–0505. Considering the solid solubility of praseodymium and neodymium oxides due to similar ionic radii and electronic configurations of Nd and Pr (Rajendran et al., 1998), the broad peaks corresponding to oxides could signify variations in stoichiometry or crystalline structure. Parts of the diffraction patterns close to the (110) peak for the bcc iron ($2\Theta \approx 44.7°$)

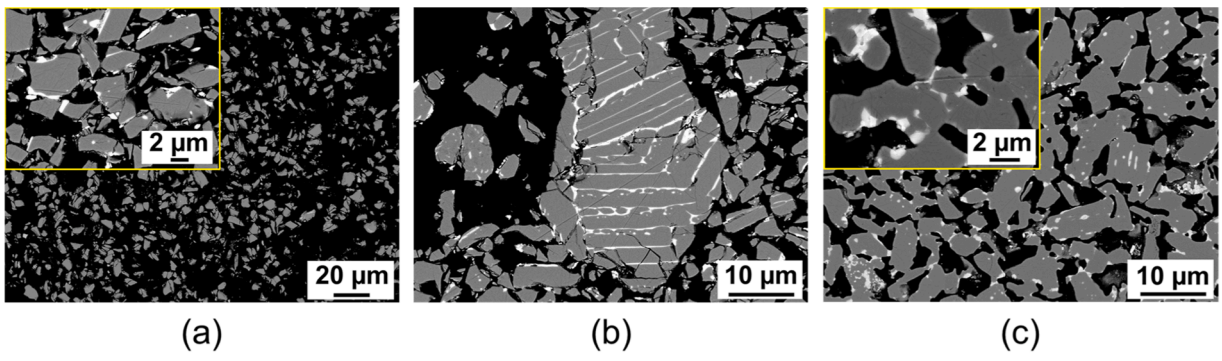

Fig. 2. Backscattered-electron (BSE) mode SEM images of the Nd-Fe-B material. (a) Initial Nd-Fe-B powder embedded in resin with a higher-magnification image shown in the inset. (b) Polycrystalline powder particle. (c) Thermally pre-treated (partially sintered) powder compact with a higher-magnification image shown in the inset.

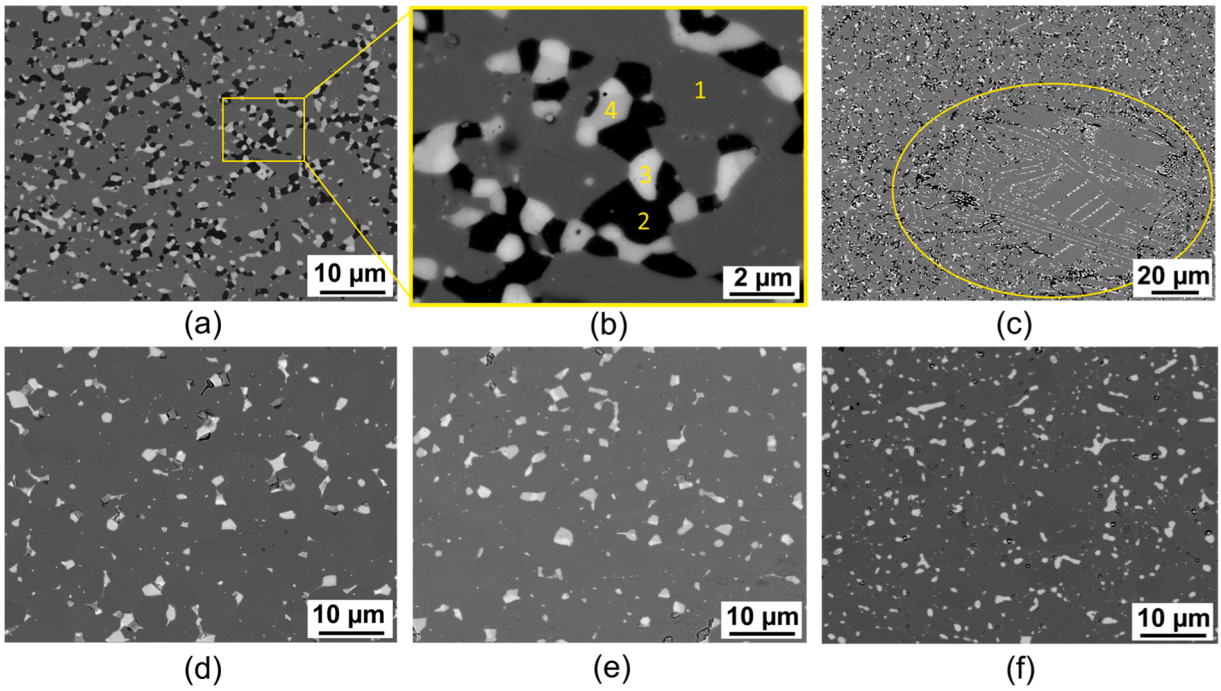

Fig. 3. BSE-SEM images taken on the FAST samples' cross-sections. (a) Sample G and (b) higher-magnification image of sample G with marked locations of EDS local compositional analyses. (c) Microstructural inhomogeneity observed in sample G. (d) Sample G-TP – prepared from a thermally pre-treated powder compact. (e) Sample G-slow – prepared with a reduced heating rate. (f) Sample W – prepared with WC die.

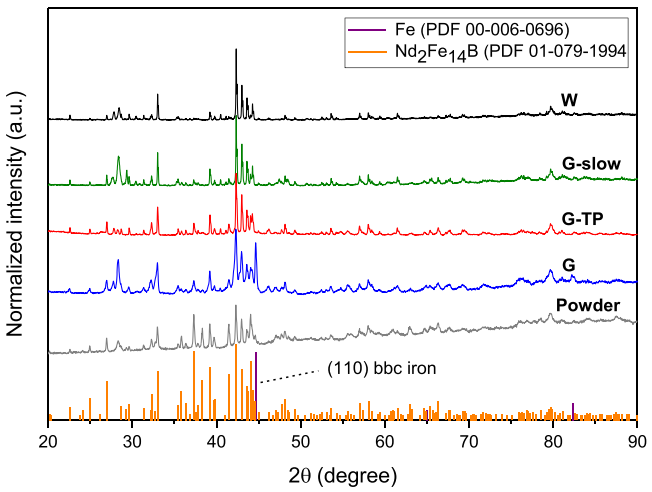

Fig. 4. X-ray diffraction patterns of the Nd-Fe-B powder and FAST samples G, G-TP, G-slow, and W. Stick patterns of the $Nd_2Fe_{14}B$ matrix phase (reference code 01–079-1994) and the bcc iron (reference code 00–006-0696) are added for comparison.

are shown in Fig. 5b. The (110) peak is pronounced in the pattern recorded for sample G and absent in other FAST samples. The results of the XRD analyses agree with that of the SEM investigation (Fig. 3), confirming that sample G contains α-Fe and that this phase is absent in samples G-TP, G-slow, and W.

3.2. Densification study and electric current

Fig. 6a illustrates the FAST process corresponding to sample G. The solid blue curve is the shrinkage curve with respect to time and the dashed red curve is the die's temperature. The slope of the shrinkage curve is positive throughout step 1 (heating), meaning that the pristine compact experienced shrinkage practically from room temperature. The temperature overshoot at T_{FAST} (950 °C) observed as a small kink in the dashed red curve at the beginning of step 2 (isothermal), was less than 10 °C. At T_{FAST}, the position of the ram becomes constant, indicating that the densification is finished. This agrees with the absence of pores (Fig. 3a) and with the high density (7.65 g/cm^3) of sample G. Fig. 6b compares the shrinkage curves with respect to the temperature for samples G (pristine compact, blue curve) and G-TP (thermally pre-treated compact, red curve). A prominent knee in the blue curve at ≈575 °C signifies an increase in the densification kinetics following the initial shrinkage. The slope of the red curve is negative from room temperature to 470 °C, meaning that at the beginning of the heating in FAST, the thermally pre-treated compact expanded. Unlike the blue curve, the red curve is convex from room temperature to ≈900 °C, where it levels off towards the end of the densification. The preceding thermal treatment of the compact therefore notably influenced the subsequent densification in the FAST. The Δd curve (dotted black curve in Fig. 6b) was constructed by subtracting the red curve from the blue curve. The slope of the Δd curve is positive from room temperature to 700 °C, and negative in the range 700–920 °C.

Fig. 7a shows the first derivatives (dy/dT) of the shrinkage curves with respect to the temperature for samples G (blue curve) and G-TP (red curve). The blue curve is characterized by two inflection points at 660 and 780 °C, signifying a decrease and an increase in the densification rate, respectively, for the pristine powder compact. This feature is absent in the red curve where only a kink can be observed at ≈660 °C. For both curves, an additional inflection point is found at ≈870 °C, as the densification rate finally decreases towards the end of step 1 (heating) of the FAST process.

The microstructures of samples G500 (Fig. 7b) and G800 (Fig. 7c) present a ''frozen'' state at 500 and 800 °C of T_{FAST}, respectively, for the pristine powder compact. The dark contrast in the BSE-SEM images is pores filled with the resin that was used to embed the samples for the analysis. During heating to 500 °C, a small number of necks were formed between the powder particles, as indicated by the arrows in Fig. 7b. The particles display a similar irregular shape as for the initial powder (Fig. 2a). Furthermore, a comparison of Fig. 2a and Fig. 7b reveals no

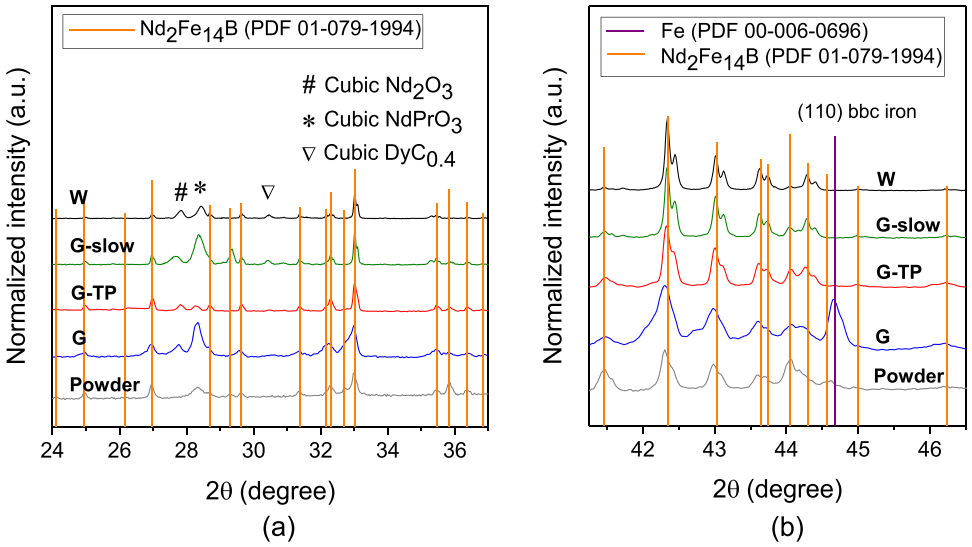

Fig. 5. X-ray diffraction patterns and phase identification. (a) 2Θ = 24–37° range with peaks corresponding to minor phases – Nd_2O_3, $NdPr0_3$, and $DyC_{0.4}$. (b) Identification of α-Fe in sample G based on the (110) peak.

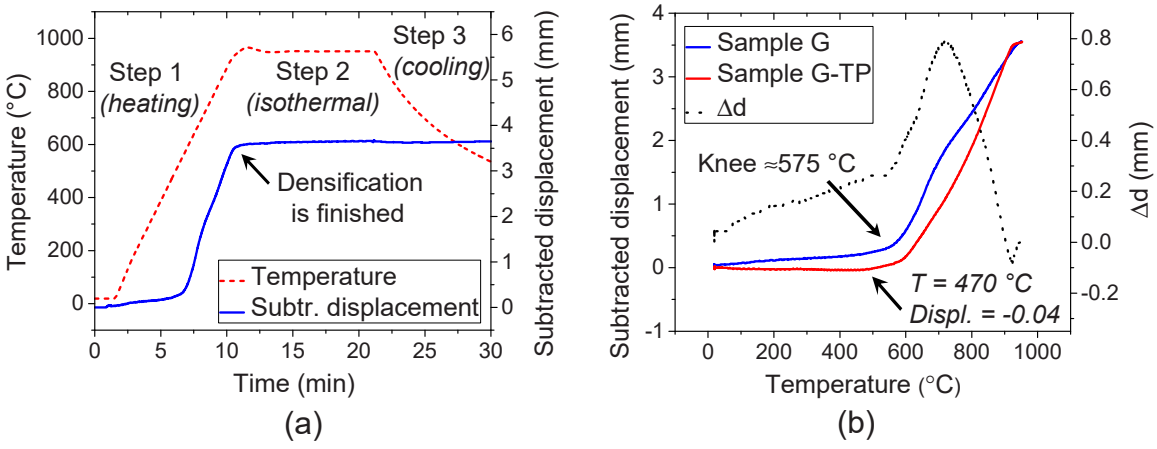

Fig. 6. FAST runs corresponding to graphite die and fast heating rate (100 °C/min). (a) Illustration of the FAST process for sample G: shrinkage curve (blue curve) and temperature of the graphite die (dashed red curve) with respect to time with marked sintering steps (heating – step 1, isothermal – step 2, and cooling – step 3). (b) Shrinkage curves for samples G and G-TP with respect to the temperature. Δd curve was constructed by subtracting the red curve (sample G-TP) from the blue curve (sample G).

signs of melting and redistribution of the bright Nd-rich phase for sample G500, and the Nd-rich phase is absent in the neck regions. The SEM investigation of sample G800 (Fig. 7c) revealed reduced porosity and two other important microstructural characteristics that were not observed for sample G500. First, the bright Nd-rich phase is redistributed, which indicates melting via the eutectic reaction (Eq. (2)), as expected for $T_{FAST} > T_{EUT}$. Secondly, α-Fe grains were observed at some of the grain boundaries and a cluster of small (<0.5 μm) α-Fe and Nd-rich grains is shown in the encircled area in Fig. 7c. An X-ray analysis confirming the α-Fe phase in similarly-prepared samples was published previously (Tomše et al., 2020).

Fig. 8a shows displacement curves with respect to temperature for samples G (blue curve), G-TP (red curve), G-slow (green curve), and W (black curve). From room temperature to approx. 500 °C, the slopes of all the curves are negative, because in this temperature range the thermal expansion of the die and spacers dominates over the shrinkage of the powder compact. For sample G-TP, the ram displacement is the most negative. This is in accordance with the absence of the sintering shrinkage, as already deduced from the shrinkage curve in Fig. 6b. All the slopes become positive at ≈550 °C when the shrinkage of the Nd-Fe-B material exceeds the thermal expansion. Fig. 8b shows the first derivatives (dy/dT) of the displacement curves with respect to the temperature. Importantly, for sample G, the blue curves in Fig. 7a (a derivative of the shrinkage curve) and Fig. 8b (a derivative of the displacement curve) are nearly identical. This is because the thermal expansion along the pressing direction is much smaller than the shrinkage of the compact due to sintering in the relevant temperature interval, making the displacement and the shrinkage curves, as well as their derivatives, comparable. As seen in Fig. 8b, densification slows down at 660 °C and increases again at ≈760–790 °C for samples G, G-slow, and W (blue, green, and black curves, respectively). The time-dependent displacement curves and temperature of the die for the FAST runs corresponding to samples G and W are shown in Fig. 8c. The full black curve (sample W) is shifted to the right, indicating a delay in densification compared to sample G (full blue curve). For the latter, the curve levels off at ≈950 °C, signifying that the densification is finished. At this temperature, the normalized ram displacement is only 0.92 for sample W and is increasing until the densification of the powder compact in the WC die is finished at ≈1000 °C. Fig. 8d compares the temperature-dependent electric current profiles for the samples

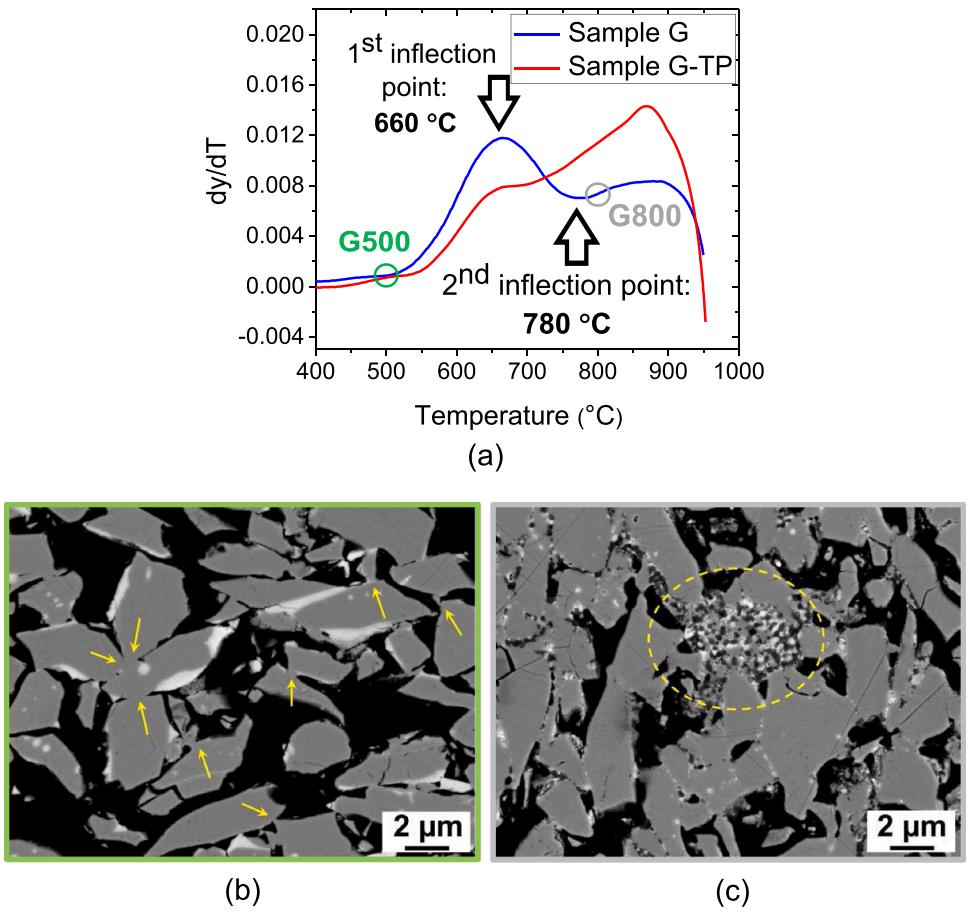

Fig. 7. Derivatives of the shrinkage curves for samples G and G-TP and microstructural changes during FAST for a pristine powder compact. (a) First derivatives (dy/dT) of the shrinkage curves with marked inflection points indicating a reduced densification rate in the range 660–780 °C for sample G. (b) BSE mode SEM image of sample G500 prepared at 500 °C. (c) BSE mode SEM image of sample G800 prepared at 800 °C.

prepared with the graphite die: G (full blue curve), G-TP (dashed red curve), and G-slow (dotted green curve). In all cases, the current steadily increases with temperature. The highest current can be observed for sample G-TP throughout the heating. For sample G-slow, the current is decreased compared to sample G.

4. Discussion

4.1. Sample's average temperature (T_A)

Considering Eq. (2), the presence of the α-Fe phase in FAST sample G, identified through SEM investigation (Fig. 3a-c) and confirmed with XRD analysis (Fig. 5b) indicates that the peritectic temperature T_{PER} (≈1180 °C) was exceeded during heating since this phase was not observed in the powder (Fig. 2a, b). A stereological analysis of the BSE-SEM images of the bulk FAST samples revealed that the area fraction of the matrix phase in sample G (≈85 %) is reduced compared to samples G-TP, G-slow, and W (≈95 %), where no α-Fe phase was observed in the microstructure. Moreover, the area fraction of the Nd-rich phases is approx. 8 % for sample G and 5 % for samples G-TP, G-slow, and W. Results of the analysis therefore confirm that the origin of the α-Fe phase is the decomposition of the matrix phase, which also increases the volume fraction of the phases rich in Nd, according to Eq. (1). Sample G was prepared at T_{FAST} = 950 °C, which is approx. 200 °C below T_{PER}. T_{FAST} is the temperature of the graphite die and the actual sample's average temperature (T_A) during FAST is not known. For any FAST process, the temperature profiles and gradients in the setup (sample and die) during heating can be significant. Electrically conductive powders might experience several tens of degrees higher temperatures than the die ($T_A > T_{FAST}$) due to a preferential current flow through the compact and direct Joule heating of the latter (Vanmeensel et al., 2005). Accordingly, the presence of α-Fe in sample G could be explained by T_A exceeding T_{PER}. However, no α-Fe phase was observed for sample G-TP (Fig. 3d) prepared from a thermally pre-treated powder compact using the same FAST parameters (Table 1). The absence of the α-Fe phase in sample G-TP reveals that T_A did not exceed T_{PER}. Importantly, for a pristine powder compact, α-Fe already forms at T_{FAST} as low as 800 °C (sample G800, Fig. 7c). It is also important to note that a local melting of the Nd-Fe-B and the subsequent precipitation of α-Fe grains upon cooling cannot be attributed to mechanical effects, i.e., high local pressure at the particle-particle contacts, as no α-Fe was observed for samples G-slow and W prepared from pristine powder compacts under the same uniaxial pressure (50 MPa) as sample G. Furthermore, the existence of plasma during FAST (*''spark-plasma sintering''* - SPS), which could explain the temperature inhomogeneities in the powder compact on the microscale during heating, was convincingly shown to be highly unlikely by Hulbert et al. (Hulbert et al., 2008). Therefore, the decomposition of the $RE_2Fe_{14}B$ matrix phase and the formation of α-Fe must be intrinsically linked to the FAST-specific processing conditions, i.e., the electrical effects associated with Joule heating.

4.2. Local overheating by the Joule effect

At the very early FAST stages, before the necks between the powder particles are formed or when their diameter is still comparatively small, the electric current flows on the surfaces of the electrically conductive

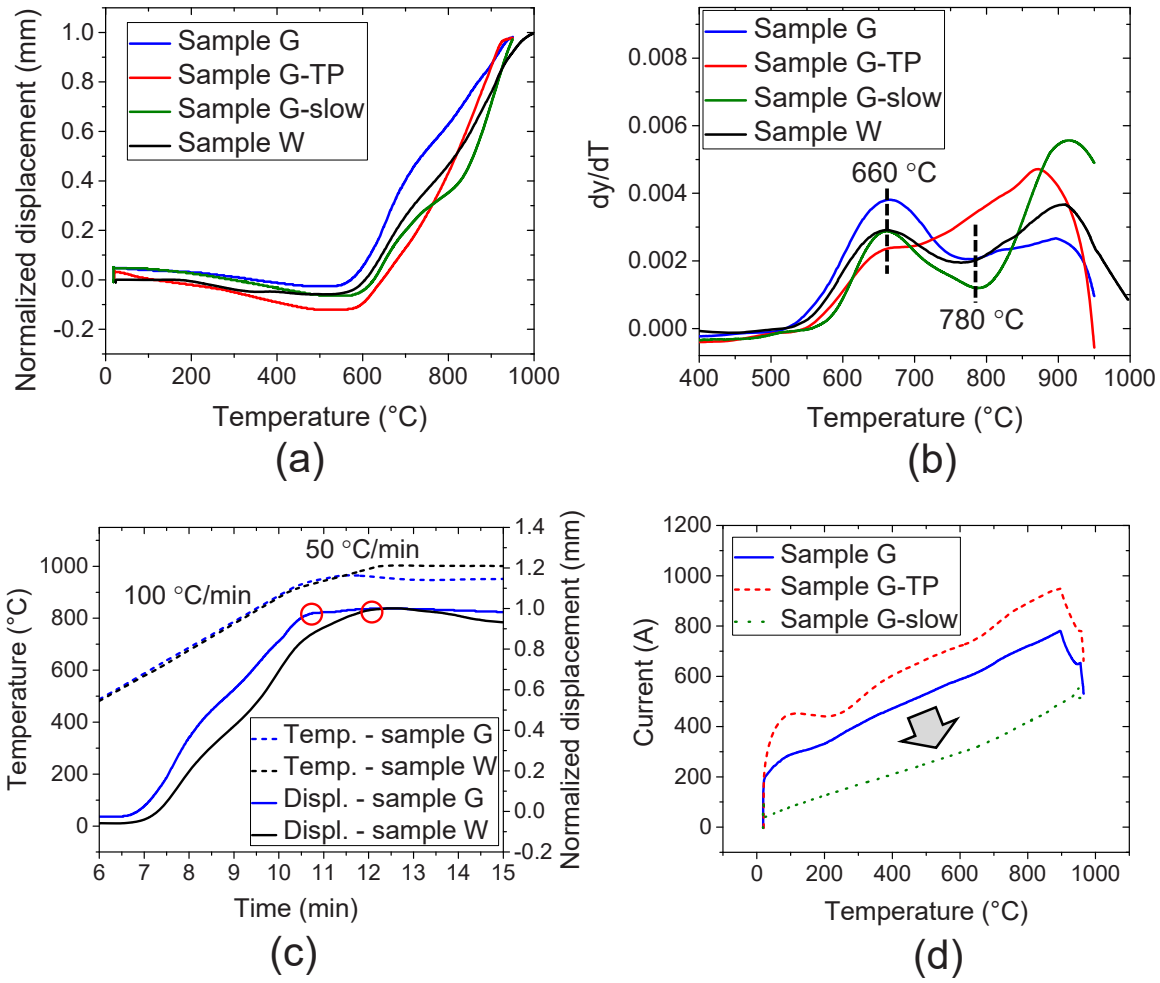

Fig. 8. Comparison of densification behaviour and electric-current profiles for samples prepared under various conditions. (a) Displacement curves with respect to temperature for samples G, G-TP, G-slow, and W. (b) First derivatives (dy/dT) of the displacement curves. The inflection points close to 660 and 780 °C are indicated with dashed vertical lines. (c) Displacement curves and temperature of the die for FAST runs corresponding to sample G (graphite die) and sample W (WC die) in relation to time; the red circles indicate the end of densification. (d) Temperature-dependent electric-current profiles for samples G, G-TP, and G-slow prepared with graphite die.

powder particles, and the heating power is dissipated at the particle-particle contacts (Suárez et al., 2013). It was theoretically predicted that in the case of TiAl powders, the current density in the contact zones is 20,000 times higher than on average in a sample (Collard et al., 2017). Arguably, a large current density can result in local overheating (''hot spots''). Song et al. (Song et al., 2006) calculated the temperature increase at the particle-particle contacts to be close to 3000 °C, as compared to only approx. 30 °C at the centre of the particle for a pulsed current passing through two contacting Cu particles having a diameter of the order of 10 μm. For their calculations, the authors considered an applied electric current of 1000 A, and a 12:2 ON/OFF pulse sequence, typical of a realistic FAST heating regime and comparable to the conditions used in our study (Section 2.2.). On the other hand, Collard et al. (2017) argued that the heat dissipation by conduction within micron-sized particles renders the actual overheating negligible, as the typical time to homogenize the particle's temperature is of the order of 5 μs; the overheating is significant only when the particle size is increased. In summary, the factors to be considered when addressing the phenomenon of local overheating are the electrical and thermal conductivities of the sintered material, the particle size, the electric-current intensity, and the pulse sequence. Electrical conductivity predetermines the preferred current path in the setup, while the thermal conductivity and the particle size are important for potentially negating the local Joule overheating that primarily depends on the FAST current. Regarding the pulse sequence, for a pulse duration of 3.3 ms, the 12:2 ON/OFF sequence used in this study translates to 12×3.3 ms ≈ 0.04 s of current, followed by 2×3.3 ms ≈ 0.007 s of pause. Even if a rapid heat conduction within a particle is assumed, the FAST heating is based on a succession of short electric pulses, each of them momentarily increasing the temperature of the particle-particle contacts. Importantly, the extent of a local temperature increase due to overheating cannot be experimentally assessed.

Local overheating by the Joule effect is the proposed mechanism for the decomposition of the $RE_2Fe_{14}B$ matrix phase during the FAST of Nd-Fe-B-type micron-sized powder. Considering the morphology of the powder particles, notably the irregular shape (Fig. 2a), the high current density is expected at particle-particle contacts, and consequently, large local thermal gradients, before the necks are formed. The microstructural investigation of the FAST samples prepared under varying conditions and their densification behaviour study were performed to support this assertion. The presence of the α-Fe phase in sample G indicates that the heat dissipation within the particles during the OFF times (between the electric pulses) was not fast enough to prevent overheating and kinetically circumvent the equilibrium phase diagram of the Nd-Fe-B system. The SEM investigation revealed that α-Fe was generally evenly distributed throughout sample G's microstructure. The few exceptions where this phase is absent are distinct regions corresponding to larger primary polycrystalline powder particles (Fig. 3c). The existence of such

microstructural inhomogeneities in a bulk FAST sample implies that the temperature in the larger particles does not exceed T_{PER} during heating, meaning that the temperature field in the compact is nonhomogeneous on a microscopic scale. Moreover, as seen in Fig. 3c, the outline of the large primary particle is easily discerned by the presence of α-Fe grains, evidencing that the FAST-induced decomposition of the $RE_2Fe_{14}B$ matrix phase occurs at the particle-particle contacts.

4.3. Effect of micro-nonuniform heating on the densification behavior

Analyses of the ram-displacement data for the FAST runs of pristine powder compacts (samples G, G-slow, and W) revealed that the densification progressed in stages. For sample G, the initial shrinkage from room temperature to ≈575 °C (Fig. 6a,b) is attributed to the formation of necks between the powder particles, as observed in the SEM image of sample G500 prepared at $T_{FAST} = 500$ °C (Fig. 7b). At this temperature, the ram displacement due to the shrinkage is 0.25 mm. Relative to the maximum ram displacement at $T_{FAST} = 950$ °C when the powder compact is densified (3.66 mm), the relative shrinkage is only 6.8 %, in agreement with the high porosity. Furthermore, as evident in Fig. 7b, the liquid phase does not yet appear at 500 °C. This agrees with T_{FAST} being significantly below the eutectic temperature T_{EUT} of the Nd-Fe-B system (655 °C) and proves that at this stage of sintering, the T_A does not exceed T_{FAST} by more than 150 °C. The prominent knee at ≈575 °C in the shrinkage curve in Fig. 6b is due to the formation of the liquid phase, which increases the densification kinetics via liquid-phase sintering. An analysis of the first derivative of the shrinkage curve (Fig. 7a) revealed that the densification rate subsequently decreases at 660 °C and increases again at 780 °C. The same trend was observed for the first derivative of the displacement curves for all the FAST samples prepared from pristine powder compacts, with only a small variation in the position of the inflection points (Fig. 8b). Furthermore, all the corresponding displacement curves displayed a similar double-S shape in the ≈600–900 °C range (Fig. 8a). Notably, the displacement curve of sample G-slow is shifted to lower values compared to sample G. Because higher heating rates favourably affect the sintering shrinkage (Roura et al., 2002), sample G densifies faster than sample G-slow.

The sintering is primarily a thermally activated process and the densification kinetics are temperature dependent. In this regard, for fixed FAST parameters such as heating rate and applied pressure, the microstructure formation and consequently the sintering shrinkage are temperature-specific. Correspondingly, the densification of a thermally pre-treated powder compact (sample G-TP) initiates at higher temperatures compared to a pristine compact (sample G), as seen in Fig. 6b and described in Section 3.2. This is ascribed to the partially sintered microstructure before the FAST, notably the presence of necks in the pre-treated compact (Fig. 2c), which hinders the initial shrinkage during FAST. Importantly, reduced densification in the 660–780 °C range for the pristine powder compact is indicative of a nonequilibrium microstructure evolution (in terms of T_A) ascribed to local overheating at the particle-particle contacts by the Joule effect, as was not observed for the thermally pre-treated powder compact (red curve in Fig. 7a). Due to the overheating, the mechanisms controlling densification, i.e., grain-boundary and lattice diffusion (Kang, 2004), are relevant for lower T_A values than would be expected for a homogeneous temperature field in a sample. Joule heating expressed at the particle-particle contacts accelerates interparticle necking, initiating shrinkage of the compact at $T_A <$ 575 °C. However, the contribution of the external pressure to this initial densification cannot be excluded. As the temperature increases, the number of necks and their diameter grow, and the local current density at neck regions is reduced. Consequently, the temperature field in the sample becomes more homogeneous, and when the local overheating diminishes, the densification slows. This leads to a shift in the trend of the Δd curve in Fig. 6b at 700 °C, signifying faster densification at $T_{FAST} <$ 700 °C, followed by reduced densification kinetics at $T_{FAST} >$ 700 °C of a pristine compact compared to the pre-treated compact. Note that this temperature is 40 °C higher than the first inflection point in the blue curve (sample G) in Fig. 7a, due to the kink in the red curve (sample G-TP) at ≈660 °C. In summary, reduced densification kinetics between 660 and 780 °C, observed for a pristine powder compact, is explained by a reduced sintering activity in this temperature range, which is a consequence of the earlier microstructure development due to local overheating.

4.4. Electric current and microstructure formation

If the high current density at particle-particle contacts for the initial FAST stages causes local overheating due to the Joule effect, reducing the current at contacts should suppress the decomposition of the matrix phase. To corroborate this logic, the significance of the (i) heating rate, (ii) the pressing tools' electrical conductivity, and (iii) the contact resistance for the microstructure formation was evaluated, and the results of the investigation presented in Section 3 are further discussed in the following.

i) For sample G-slow, the heating rate was reduced by an order of magnitude, from 100 to 10 °C/min. According to Eq. (3), the current grows as the square root of the power required to heat the setup (sample and die) to the target temperature if the temperature dependence of the resistance is assumed to be negligible. Slower heating requires less power and accordingly, the FAST current decreased (Fig. 8d), which resulted in an α-Fe free microstructure (Fig. 3e). While the modified FAST conditions affected the final phase composition, slower heating did not influence the density, as both samples, prepared either by fast (sample G) or slow heating (sample G-slow), were fully dense.

ii) To prepare sample W, an electrically highly-conductive WC die and insulating BN coating were used (Section 2.2.), imitating conditions similar to FAST of electrically nonconductive materials where the die is heated by the Joule effect and the sample is heated indirectly through thermal conduction (Vanmeensel et al., 2005). The replacement of the graphite with the WC die influenced the densification. In the WC case, the displacement curve is shifted to the right (densification is delayed) for the same heating rate (Fig. 8c), which agrees with increased current flow through the more conductive WC die, effectively raising its temperature relative to that of the sample. In other words, for the same T_{FAST}, T_A is lower when WC is used instead of graphite. Consequently, approx. 50 °C higher T_{FAST} was required to densify the powder compact. In agreement with i), reducing the current flow through the sample by increasing the electrical conductivity of the pressing tools and using the BN protective coating favourably altered the microstructure formation, inhibiting the decomposition of the matrix phase (Fig. 3f).

iii) The heating power is comparable between the FAST runs corresponding to sample G and sample G-TP since all the relevant FAST parameters (heating rate, T_{FAST}, dimensions of the setup, material of the pressing tools, and the sample's weight) are the same. Because the square of the current and the resistance are inversely proportional (Eq. (3)), the higher current recorded for the FAST run corresponding to sample G-TP (Fig. 8d) is attributed to the decreased electrical resistance of the pre-treated powder compact. The necks between the powder particles observed for the latter (Fig. 2c) act as paths for the electric current, which diminishes the contribution of the interparticle contact resistance to the overall electrical resistance of the material. Reducing the contact resistance and thereby the current density at particle-particle contacts prevented the peritectic decomposition of the matrix phase in sample G-TP (Fig. 3d).

5. Conclusions

The hypothesis of local overheating at the particle-particle contacts by the Joule effect during field-assisted sintering (FAST) was validated for a multiphase, microcrystalline, Nd-Fe-B-type metallic powder. A peritectic decomposition of the $RE_2Fe_{14}B$ matrix phase at ≈1180 °C, leading to the precipitation of α-iron, was applied as an indicator for the micro-nonuniform heating. The SEM investigation revealed that the α-Fe forms at particle-particle contacts, confirming that the sample's average temperature is exceeded in the contact regions during heating.

Practical solutions were proposed to overcome the adverse effects of local overheating on microstructure formation without decreasing the sintering temperature or compromising the final density. Decreasing the current in the sample by reducing the heating rate or increasing the electrical conductivity of the pressing tools mitigates the impact of local overheating on phase formation and prevents the presence of α-Fe in the final samples. Similarly, the overheating is greatly diminished in a powder compact partially pre-sintered before FAST, which is attributed to the minimized electric current density in the neck regions.

For the Nd-Fe-B system, micro-nonuniform heating affects the densification behaviour, resulting in a characteristic double-S shape of the displacement curves, irrespective of the final phase composition of the samples prepared from the pristine powder compacts. Two conclusions can be drawn from this. Firstly, reducing the current does not eliminate the local overheating by the Joule effect, but rather reduces the local temperature increase at particle-particle contacts. Secondly, the micro-nonuniform heating is inherent to the FAST. Although its significance may be marginal for electrically non-conductive ceramics, it necessitates consideration for further development of the FAST-based sintering strategies for metallic powders.

CRediT authorship contribution statement

Benjamin Podmiljšak: Methodology, Investigation. **Tomaž Tomše:** Writing – review & editing, Writing – original draft, Methodology, Investigation, Conceptualization. **Andraž Kocjan:** Validation, Writing – review & editing. **Spomenka Kobe:** Methodology, Validation. **Reto Kessler:** Validation, Investigation. **Lavinia Scherf:** Validation, Investigation. **Kristina Žužek:** Supervision, Writing – review & editing. **Sašo Šturm:** Methodology, Writing – review & editing.

Declaration of Competing Interest

The authors declare that they have no known competing financial interests or personal relationships that could have appeared to influence the work reported in this paper.

Acknowledgment

This research was funded by Slovenian Research and Innovation Agency (research core funding no. P2–0084, and project Z2–2645), EIT RAW Materials RECO2MAG (grant agreement no. 21043), and European Union's Horizon Europe Research and Innovation Program REESILIENCE (grant agreement no. 101058598). The authors also acknowledge financial support from the World Federation of Scientists (WFS) through National Scholarship Programme. Monika Kušter is acknowledged for technical assistance.

References

Bernardi, J., Fidler, J., Sagawa, M., Hirose, Y., 1998. Microstructural analysis of strip cast Nd–Fe–B alloys for high (BH) max magnets. J. Appl. Phys. 83 (11), 6396–6398. https://doi.org/10.1063/1.367557.

Burzo, E., 1998. Permanent magnets based on R-Fe-B and R-Fe-C alloys. Rep. Prog. Phys. 61, 1099–1266. https://doi.org/10.1088/0034-4885/61/9/001.

Collard, C., Trzaska, Z., Durand, L., Chaix, J.-M., Monchoux, J.-P., 2017. Theoretical and experimental investigations of local overheating at particle contacts in spark plasma sintering. Powder Technol. 321, 458–470. https://doi.org/10.1016/j.powtec.2017.08.033.

Guillon, O., Gonzalez-Julian, J., Dargatz, B., Kessel, T., Schierning, G., Räthel, J., Herrmann, M., 2014. Field-assisted sintering technology/spark plasma sintering: mechanisms, materials, and technology developments. Adv. Funct. Mater. 16 (7), 830–849. https://doi.org/10.1002/adem.201300409.

Herbst, J., 1991. R 2 Fe 14 B materials: intrinsic properties and technological aspects. Rev. Mod. Phys. 63 (4), 819. https://doi.org/10.1103/RevModPhys.63.819.

Holland, T.B., Anselmi-Tamburini, U., Quach, D.V., Tran, T.B., Mukherjee, A.K., 2012. Effects of local Joule heating during the field assisted sintering of ionic ceramics. J. Eur. Ceram. Soc. 32 (14), 3667–3674. https://doi.org/10.1016/j.jeurceramsoc.2012.02.033.

Hulbert, D.M., Anders, A., Dudina, D.V., Andersson, J., Jiang, D., Unuvar, C., Anselmi-Tamburini, U., Lavernia, E.J., Mukherjee, A.K., 2008. The absence of plasma in "spark plasma sintering. J. Appl. Phys. 104 (3), 033305 https://doi.org/10.1063/1.2963701.

S.-J.L. Kang, Sintering: densification, grain growth and microstructure, Elsevier2004.

Lewis, L.H., Jiménez-Villacorta, F., 2013. Perspectives on permanent magnetic materials for energy conversion and power generation. Metall. Mater. Trans. A 44 (1), 2–20. https://doi.org/10.1007/s11661-012-1278-2.

Liu, W., Cui, Z., Yi, X., Yue, M., Jiang, Y., Zhang, D., Zhang, J., Liu, X., 2010. Structure and magnetic properties of magnetically isotropic and anisotropic Nd–Fe–B permanent magnets prepared by spark plasma sintering technology. J. Appl. Phys. 107 (9) https://doi.org/10.1063/1.3339067.

Manière, C., Nigito, E., Durand, L., Weibel, A., Beynet, Y., Estournès, C., 2017. Spark plasma sintering and complex shapes: the deformed interfaces approach. Powder Technol. 320, 340–345. https://doi.org/10.1016/j.powtec.2017.07.048.

Matsuura, Y., Hirosawa, S., Yamamoto, H., Fujimura, S., Sagawa, M., Osamura, K., 1985. Phase diagram of the Nd-Fe-B ternary system. Jpn. J. Appl. Phys. 24 (8A), L635. https://doi.org/10.1143/JJAP.24.L635.

Mazo, I., Molinari, A., Sglavo, V.M., 2022. Electrical resistance flash sintering of tungsten carbide. Mater. Des. 213, 110330 https://doi.org/10.1016/j.matdes.2021.110330.

Nowak, S., Perrière, L., Dembinski, L., Tusseau-Nenez, S., Champion, Y., 2011. Approach of the spark plasma sintering mechanism in Zr57Cu20Al10Ni8Ti5 metallic glass. J. Alloy. Compd. 509 (3), 1011–1019. https://doi.org/10.1016/j.jallcom.2010.09.158.

Orru, R., Licheri, R., Locci, A.M., Cincotti, A., Cao, G., 2009. Consolidation/synthesis of materials by electric current activated/assisted sintering. Mater. Sci. Eng. R. Rep. 63 (4-6), 127–287. https://doi.org/10.1016/j.mser.2008.09.003.

Rajendran, M., Mallick, K., Bhattacharya, A., 1998. Preparation and characterization of LnPrO3+ y (Ln= Y and lanthanide)—a series of mixed lanthanide oxides. Mater. Lett. 37 (1-2), 10–16. https://doi.org/10.1016/S0167-577X(98)00058-5.

Roura, P., Costa, J., Farjas, J., 2002. Is sintering enhanced under non-isothermal conditions? Mater. Sci. Eng. A 337 (1), 248–253. https://doi.org/10.1016/S0921-5093(02)00029-1.

Ruoho, S., Haavisto, M., Takala, E., Santa-Nokki, T., Paju, M., 2010. Temperature dependence of resistivity of sintered rare-earth permanent-magnet materials. IEEE Trans. Magn. 46 (1), 15–20. https://doi.org/10.1109/TMAG.2009.2027815.

Sagawa, M., Fujimura, S., Togawa, N., Yamamoto, H., Matsuura, Y., 1984. New material for permanent magnets on a base of Nd and Fe. J. Appl. Phys. 55 (6), 2083–2087. https://doi.org/10.1063/1.333572.

Sagawa, M., Hirosawa, S., Tokuhara, K., Yamamoto, H., Fujimura, S., Tsubokawa, Y., Shimizu, R., 1987. Dependence of coercivity on the anisotropy field in the Nd2Fe14B-type sintered magnets. J. Appl. Phys. 61 (8), 3559–3561. https://doi.org/10.1063/1.338725.

Schultz, L., El-Aziz, A.M., Barkleit, G., Mummert, K., 1999. Corrosion behaviour of Nd–Fe–B permanent magnetic alloys. Mater. Sci. Eng. A 267 (2), 307–313. https://doi.org/10.1016/S0921-5093(99)00107-0.

Schwesig, D., Schierning, G., Theissmann, R., Stein, N., Petermann, N., Wiggers, H., Schmechel, R., Wolf, D., 2011. From nanoparticles to nanocrystalline bulk: percolation effects in field assisted sintering of silicon nanoparticles. Nanotechnology 22 (13), 135601. https://doi.org/10.1088/0957-4484/22/13/135601.

Song, X., Liu, X., Zhang, J., 2006. Neck formation and self-adjusting mechanism of neck growth of conducting powders in spark plasma sintering. J. Am. Ceram. Soc. 89 (2), 494–500. https://doi.org/10.1111/j.1551-2916.2005.00777.x.

Suárez, M., Fernández, A., Menéndez, J., Torrecillas, R., Kessel, H., Hennicke, J., Kirchner, R., Kessel, T., 2013. Challenges and opportunities for spark plasma sintering: a key technology for a new generation of materials, 13, 319–342. https://doi.org/10.5772/53706.

Tomše, T., Samardžija, Z., Scherf, L., Kessler, R., Kobe, S., Rožman, K.Ž., Šturm, S., 2020. A spark-plasma-sintering approach to the manufacture of anisotropic Nd-Fe-B permanent magnets. J. Magn. Magn. Mater. 502, 166504 https://doi.org/10.1016/j.jmmm.2020.166504.

Trzaska, Z., Collard, C., Durand, L., Couret, A., Chaix, J.M., Fantozzi, G., Monchoux, J.P., 2019. Spark plasma sintering microscopic mechanisms of metallic systems: experiments and simulations. J. Am. Ceram. Soc. 102 (2), 654–661. https://doi.org/10.1111/jace.15999.

Uestuener, K., Katter, M., Rodewald, W., 2006. Dependence of the mean grain size and coercivity of sintered Nd–Fe–B magnets on the initial powder particle size. IEEE Trans. Magn. 42 (10), 2897–2899. https://doi.org/10.1109/TMAG.2006.879889.

Vanmeensel, K., Laptev, A., Hennicke, J., Vleugels, J., Van der Biest, O., 2005. Modelling of the temperature distribution during field assisted sintering. Acta Mater. 53 (16), 4379–4388. https://doi.org/10.1016/j.actamat.2005.05.042.